Image-based measurement of flux variation in distal regions of active lava flows.

James, M.R.[1], Pinkerton, H.[1], and Robson, S.[2],

[1]Lancaster Environment Centre, Lancaster University, Lancaster LA1 4YQ, U.K.

[2]Department of Geomatic Engineering, University College London, London. WC1E 6BT, U.K.

Abstract

Understanding the processes involved with the advance of lava flows is critical for improving hazard assessments at many volcanoes. Here, we describe the application of computer vision and oblique photogrammetric techniques to visible and thermal images of active 'a'ā flows in order to investigate distal flow processes at Mount Etna, Sicily. Photogrammetric surveys were carried out to produce repeated topographic datasets for calculation of volumetric lava flux at the flow-fronts. Velocity profiles from a distal channel were obtained by rectification of a thermal image sequence and are used to investigate the rheological properties of the lava. Significant variations of the magma flux were observed, and pulses of increased flux arrived within the flow-front region on timescales of several hours. The pulses are believed to be the distal result of more frequent flux changes observed in the vent region. Hence, they reflect the importance of flow processes which are believed to cause the coalescence of flux pulses along the channel system as well as short-period variations in effusion rate. In considering advance processes for the individual flow-fronts, it must be assumed that they were fed by a highly unsteady flux, which was volumetrically at least an order of magnitude lower than that observed near the vent.

Keywords: close-range photogrammetry, thermal imaging, lava flow, Etna, effusion rate, rheology

1 Introduction

Accurate effusion rate measurements are important during active eruptions because of their role in controlling the lengths of lava flows [*Walker*, 1973; *Pinkerton and Wilson*, 1994], surface textures [*Pinkerton and Sparks*, 1976] and the complexity of the resulting flow or flow field [*Walker*, 1972; *Kilburn and Lopes*, 1988]. However, volumetric lava flux (or flow rate) is a difficult parameter to measure accurately in the field, and on Etna, the problems are compounded by changes in flux that have been previously reported over a wide range of timescales [*Neal and Decker*, 1983; *Frazzetta and Romano*, 1984; *Guest et al.*, 1987; *Harris et al.*, 2000; *Calvari et al.*, 2002; *Lautze et al.*, 2004; *Bailey et al.*, 2006]. An example of short-term variations is given by *Lautze et al*. [2004], who report observations of unsteady flow in a proximal lava channel on Etna in 2001, characterised by 10 – 30 minute surges, interspersed between 1 – 3 hours of waning flow. Flux changes have also been observed on other volcanoes such as Arenal [*Wadge et al.*, 2006] and Mauna Loa [*Lipman and Banks*, 1987].

Although the importance of flux magnitude is clear in lava flow models, and relatively long-term flux changes have been incorporated [*Crisci et al.*, 2003; *Hidaka et al.*, 2005], the influence of this type of rapid change is not yet known. In order to improve flow models, a greater understanding of flux variations and their causes is required. Ground-based imaging using affordable digital cameras and thermal imagers now offers the opportunity to provide significant volumes of data for flow analysis. Here, oblique photogrammetric and computer vision techniques are employed to quantify advance rates, channel flow thickness and widths and similar data for flow-fronts, in distal regions of 'a'ā lava flows on Mount Etna, Sicily.

Lava flux estimates are generally made either by relatively direct point measurement of parameters such as flow velocity [e.g. *Guest et al.*, 1987; *Lipman and Banks*, 1987; *Calvari et *al.*, 2002], by differencing sequential topographic fields of the area being analysed [e.g. *Macfarlane et al.*, 2006; *Wadge et al.*, 2006] or by thermal flux techniques [*Harris et al.*, 1998; *Harris et al.*, 2000; *Harris et al.*, 2005]. The choice of method depends on the rate and area of change and the measurement frequency required. Space-based techniques or airborne imagery usually cover wide areas, but are relatively infrequently carried out as determined by overflights and cloud conditions. Hence, average flux values over intervals of days to years, are calculated from these datasets, providing useful insights into the overall behaviour of a volcano, but providing few constraints for flow models. In order to acquire significantly more frequent measurements, practicalities dictate that ground-based (and therefore usually close-range) methods are used. However, spatially extended ground-based surveys are generally slow and consequently point measurements of flux proxies (such as lava channel depth or velocity) are used where changes are of a sufficient magnitude to measure. To date, sufficiently frequent measurements to detect rapid changes in flux have been restricted to relatively fast flowing lava channels [e.g. *Guest et al.*, 1987; *Lipman and Banks*, 1987; *Bailey et al.*, 2006] and have not recorded flux variations within slower evolving regions of lava flow-fields.

Airborne laser scanners have been used to collect detailed topographic data on volcanoes [*Mazzarini et al.*, 2005]; however their deployment is expensive and they cannot image through condensing volcanic gases or cloud. Ground-based versions [*Hunter et al.*, 2003] are difficult to transport to relatively inaccessible areas and can take a significant time to acquire a large scan, limiting their use on evolving scenes. Oblique photogrammetric techniques [*Chandler et al.*, 2002; *Cecchi et al.*, 2003; *James et al.*, 2006] are significantly less expensive, easier to deploy to relatively inaccessible areas and, with careful data analysis, can produce frequent, but relatively spatially extended, volume change data for flux measurement. In the surveys described below, fluxes < 1 m^3s^{-1} were measured over spatial dimensions of order 100 m, at repeat intervals of tens of minutes to hours.

The data presented here were collected in September 2004 from 'a'ā flows on Mount Etna, Sicily. The lava flux changes measured correlate with field observations of unsteady flow behaviour which was responsible for levee building and breaching, and was hence significant in the evolution of the flow field. Such variations represent an important process which ultimately should be incorporated into numerical flow models.

2 Eruption setting

The 2004-2005 eruption of Etna started on 7 September, on the lower eastern flank of the South East Cone, and continued until 8 March at an average extrusion rate of ~3 m^3s^{-1} [*Burton et al.*, 2005]. At the time of fieldwork, lava was being erupted from two vents in the headwall of the Valle del Bove (Figure 1). 'A'ā flow-fronts from the northerly, higher vent had reached the valley floor south of Monte Centenari and were stopping close to the break in slope. Over the period of measurement, the flow-fronts observed were fed by the main channel from the northern vent, which descended the headwall (an average slope of 22°) in an easterly direction before turning south ~300 m from the active fronts. Breakouts to the northern side of the channel and at higher altitude could not be observed due to the local topography, but several were known to have occurred from observations made from the summit of Monte Centenari on 30 September.

The flow-front region was visited on 23 and 25 – 30 September, 2004 but detailed measurements were not possible on all days due to weather conditions. Over this period, a sequence of 4 active flow-fronts were observed forming from breakouts successively higher up the channel system, which then descended the lower regions of the headwall, before stalling when the local slope decreased to ~7° on the floor of the Valle del Bove.

On 23 September, a flow-front was advancing across the valley floor and was seen to be active only on that day. This flow provided the eastern boundary to subsequent flows and, by 25 September, its feeder channel was observed to be ~80 % drained and inactive. On 26 September, the next flow-front had fully developed and was descending alongside the west levee of the previous flow. This, and the subsequent two flow-fronts, were imaged and mapped over the next three days (Figures 2 and 3).

On 27 September (Figure 2b) the active flow-front of the previous day (designated as flow-front 1) had reached the flatter ground and was advancing at ~3 m hr^{-1}. Another breakout had occurred and, after a section of bifurcated channel, the new flow (flow-front 2) had started to descend along the previous western levee. By 28 September this new flow-front was the dominantly active one, although some minor advance of the previous flow-front was also detected (Figure 2c, note that the elevated temperatures in the thermal image suggest that flow-front 1 was still significantly active at the time of imaging). By the next day, both flow-fronts 1 and 2 were inactive and a new flow-front (3) had descended and was advancing at ~4 m hr^{-1} (Figure 2d). Brief observations made on the 30 September confirmed that this flow-front had travelled further than its predecessors, and halted only when it reached a topographic rise ~4 – 5 m high.

Over this period, the flows observed were typical blocky 'a'ā, ~7 m thick, 15 – 70 m wide, with active fronts inclined at ~40° to the horizontal. Flow-front advance was marked by rubble falling from the flow surface as well as periodic spalling from the flow-front, which temporarily revealed incandescent material. Ogives were visible in both channels where the flows traversed the shallow gradient of the valley floor, but were most pronounced in the channel feeding flow-front 1.

3 Imaging and Analyses

Thermal and visible images of the active flow-fronts were collected during the fieldwork period, and the images obtained on 27 – 29 September were suitable for photogrammetric analysis and topographic reconstruction. Since the lavas descended a slope onto relatively flat terrain, images acquired from in front of the flow-fronts also included some of the distal channel regions. Fortuitously, the local topography increased some distance away from the flow-fronts allowing further images to be acquired from slightly higher vantage points, increasing the area of terrain, and therefore of the flow's upper surface, which could be observed. The photogrammetric approach and techniques used have been previously described in *James et al.* [2006] but have subsequently been improved for better topography extraction. The method uses images taken by a single camera which is moved around the region being studied, in this case, the lava flow-fronts. For a survey, multiple images are acquired and, as long as this is carried out significantly faster than the timescale of change within the region, accurate photogrammetric measurements can be achieved. Each survey constitutes calculation of a photogrammetric network (i.e. calculating camera orientations and refining control target positions) from multiple images (typically 20 – 30 images), in each of which a minimum of four points of known positions (control targets) must be observable. Once this is achieved, topographic points are then calculated by image matching between a few relatively similar images within the network (Table 1), and a surface model is then constructed by interpolating the data onto a regular *x*-*y* grid. The distance between the camera positions of matched images is generally between 5 and 20 m, and was dependent on the scene being observed and the practicalities of moving over the local topography.

Visible images were taken using a 6 megapixel digital SLR camera (Canon EOS 300D) with a fixed focal length (28 mm) lens. For long distance images, a 50 mm lens was also employed. The imaging geometry of the camera and lenses had been pre-calibrated in the laboratory for photogrammetric use. Calibration confirmed that the photogrammetric imaging geometry of the camera was sufficiently well understood to deliver 3D coordinates with a precision of better than 1:60,000, a ratio representing the calculated 3D point precision with respect to the overall spatial extent of the photogrammetric coverage. In order to maintain the calibration, the mechanical focus adjustment of the lens was locked to provide sharp images over a ~5 m to infinity range at a lens aperture of f/11.

Spatial control for the photogrammetric network was provided by aluminium foil control targets. Three control networks were deployed sequentially as the flows advanced; an initial wide network of flat targets, ~40 cm across (spanning distances of up to ~200 m and originally designed to support potential helicopter-borne imaging), a intermediate network comprising foil-wrapped rocks on local topographic highs (spanning distances of up to ~100 m), and the smallest network comprising foil balls, approximately 4 cm in diameter (spanning distances of up to ~30 m). All targets were deployed on static ground and once their positions had been measured they were deemed to be in fixed positions. The wide and intermediate networks were used on 27 and 28 September for imaging flow-fronts at distances of up to ~100 m. For increased accuracy when imaging over shorter distances (~30 – 50 m), these networks were augmented by the smallest network on 29 September.

Target coordinates were obtained using GPS (a ProMarkX receiver, logging for a minimum of 15 minutes at each site) with additionally, for the two smaller networks, target-to-target distances measured with a tape measure. Tape-measured distances between targets were deemed accurate to ±10 – 20 mm depending on the line length. With both types of geometric constraint being incorporated into the photogrammetric projects, local accuracy and overall georeferencing could be achieved. However, in this work, only relative registration of the topographic data was required, consequently absolute referencing accuracy has not been assessed. Point precisions were centimetric in regions close to the camera, increasing to decimetric over the longer distances used. These precisions are significantly lower than those achievable under optimal conditions and in the laboratory, but reflect some of the difficulties in rapidly producing extended networks under field conditions.

Topographic data were obtained by using an iterative feature-based image patch matching routine [*Papadaki*, 2002] within the photogrammetric software (VMS (www.geomsoft.com), Robson & Shortis). The photogrammetric output is in the form of a point cloud (a 3D distribution of points) representing the positions of distinct features detected in the images. Outliers are initially removed by rejecting all 3D points with vertical precisions >0.5 m. Any remaining outliers (resulting from incorrectly matched points) were easily observed and manually removed within an appropriate viewer. Point clouds are then interpolated into a regular *x-y* grid to form a digital elevation model (DEM) for volumetric analysis. Two examples of such surface reconstructions are shown in Figure 4, an overview, covering the majority of the area imaged (Figure 4a), and a second, higher resolution reconstruction (interpolated onto a 20 cm grid) covering a single flow-front (Figure 4d) for flux calculation. In Figure 4d, the flow-front topography is shaded by the magnitude of change since the previous survey. The sum of these changes was used to calculate flux, with regions of negative change being generally negligible. Figure 4d shows a typical area (30 × 40 m) reconstructed for flow-front flux calculations on 29 September, when the flow-front was relatively localised (Figure 3). Wider regions (up to ~70 m across) were used for 27 and 28 September due to the larger flow-fronts active on these days.

Errors in the final surface models arise from three sources, those propagating from individual point matches, systematic errors resulting from inaccuracies in the relative camera orientations (and also from the camera model, although relative to others, these are negligible) and errors due to interpolation over data-poor areas. Of these, the first two are angular in nature and consequently, DEM accuracy decreases with distance from the camera. Using ground-based imagery for reconstructing surfaces of a braided riverbed, *Chandler et al.* [2002] were able to produce point precisions of <0.03 m over distances up to 280 m and the resulting DEMs had root mean square errors of <0.05 m. This illustrates the potential of ground-based photogrammetric methods; however these accuracies were not achieved (nor required) in this work for several reasons.

On Etna, the topography was less favourable (*Chandler et al.* [2002] were able to observe the river bed from close and steep valley sides); the very oblique views on Etna meant that control targets were at a wide range of distances from the camera and could not be optimised (for size or position) from all camera positions. The advancing flows also obscured and overran targets, so some targets had to be located in places initially away from the flows (although many were lost by 30 September), rather than in optimal positions for photogrammetry. This also meant that a wide angle lens had to be used in order to include both the flows and surrounding control targets within images, effectively decreasing the imaging resolution of the flow areas. In order to assess the repeatability of the surfaces produced, cross-sections through DEMs from three surveys on 27 September are shown in Figure 4b. The region of static ground shown was ~150 – 200 m from the camera positions, and hence >50 m farther away than the flow-fronts. To estimate error in any volumetric change calculated, the average magnitude of the mean offsets between these sections has been calculated and is 0.16 m. Similar analysis for data collected on 29 September from closer positions (~25 m) shows a mean offset of 0.02 m.

For thermal imaging, a tripod-mounted FLIR S40 was used and, on 27 September, synoptic views of the distal channel region and the active flow-fronts were recorded. Images were collected every second, but data continuity was broken during periods of obscuration by low cloud and heavy rain (during which the instrument was covered). Due to the limited spatial resolution of the thermal camera, thermal images (320 × 240 pixels) were registered to the topographic data by incorporating a visible image taken from the same position into the photogrammetry network. The camera azimuth, pitch and roll could then be determined by matching features in the thermal and associated visible image.

A thermal image sequence was used to analyse the flow of lava down a distal channel in order to assess flux and rheological properties. Although the thermal camera has a significantly lower spatial resolution than most standard cameras, the high contrast in thermal images of active 'a'ā lavas makes them ideal for monitoring the evolution of flow features. The detection and tracking of change within an image sequence is a common computer vision problem and a Lucas-Kanade ‘optical flow’ technique [*Horn and Schunck*, 1981; *Lucas and Kanade*, 1981;

Davies, 2005] was used to follow motion in image sequences. In this, for each sequential image pair, a displacement map is sought which references the pixels of one image to corresponding areas in the other, in order to minimise pixel intensity changes between the images. This essentially 'tracks' intensity values which, for the application here, describes the motion of the flow surface.

4 Observations and flux measurements

4.1 Flux pulses in channels

Pulses of lava were observed descending the distal region of the main channel on each day, with up to three being seen over the longest observation period (~9 hrs). In Figure 5, a sequence of thermal images shows the progression of a pulse through the area of bifurcated channel on 27 September. In the first panel (i), the relatively steady conditions prior to the arrival of the pulse are illustrated. The increasing lava flux associated with a pulse is initially indicated by increasing apparent temperatures and an increase in the lava depth within the channel (panel (ii), just above the bifurcation). The pulse split as it flowed into the bifurcation (iii), and the effective increase in channel area slowed the advance of the pulse front. Additional fresh material continued to flow in behind the front, inflating the flow surface (iv), sufficiently, in the flow-front 2 channel branch, to overtop the levees (v). In this channel, as the pulse front traversed a slightly shallower gradient section (~20°, vi-viii) it was simultaneously growing in height and cascading rubble over the levees, effectively levee-building as it progressed. At ~15:50 (viii) the pulse approached a steep (~30°) section of channel, accelerated rapidly and appeared to slump down the remaining channel (ix-x). Unfortunately, measurements had to be curtailed (in order to leave the area in daylight) before the effect of this pulse on the flow-front could be observed.

In the channel feeding flow-front 1, overflows did not occur due to the wider and deeper nature of the channel, but variations in channel depth are shown throughout the image sequence (see Figure 6b). It is worth noting that similar distal flux variations were observed during the Pu'u 'Ō'ō-Kūpaianaha eruption on Hawai'i, for which *Neal and Decker* [1983] describe 40-minute 'surges' of high volume and high velocity flow which represented fluxes up to an order of magnitude greater than those during 'inter-surge' periods (lasting 2 to 8 hours). However, the authors are unaware of any detailed published data on the processes involved.

4.2 Flow-front fluxes

Eleven surface models were produced of the active flow-front regions observed between 27 and 29 September. Each model was the product of one photogrammetric survey (listed in Table 1), and fluxes were calculated by subtracting the active flow-front regions of successive models. The resulting flux values (of up to 0.35 $m^3\ s^{-1}$) are given in Figure 6a, where each thick horizontal line reflect the average flux between two surveys (carried out at the times denoted by the end points of the line). None of the three monitored flow-front regions exhibited a steady evolution. Instead, the data suggest periods of both waxing and waning flux (Figure 6a) with, for example, flow-front 1 advancing at rates between 0.045 and 0.35 $m^3\ s^{-1}$.

In order to verify that these variations are real and not within measurement error, one can consider worst-case scenarios based on the measured mean surface offsets of 0.02 m (at ~25 m from the camera positions) and 0.16 m (at ~175 m from the camera positions). For example, if a survey carried out on 29 September (flow front 3, e.g. Figure 4d), was susceptible to a systematic vertical error of ~0.05 m over a typical flow-front area of ~20 × 30 m, this would represent a volume error of ±30 m^3. Thus, for a flow front advancing at ~0.2 $m^3\ s^{-1}$, surface measurements taken approximately an hour apart would show a volumetric change of 720 ± 30 m^3, representing a calculated flux error of <5 %. In Figure 6a, the width of the grey error bars have been calculated from this approach, using appropriate spatial areas, and vertical offsets of 0.05 m for the relatively close flow-fronts observed on 29 September and 0.2 m for the more distant (~100

m) flow-fronts observed on the preceding days. For the overnight advance of flow-front 2, the complete region was not fully captured in survey 28a (as demonstrated by the dashed bounding line in Figure 3), so simple geometric extrapolation had to be used between parts of surveys 27c and 28a. This has been accounted for in the error estimate by increasing the potential vertical offset between these particular surfaces to 0.5 m.

Note that the flux measurement made between surveys 29b1 and 29b2 (carried out 5 minutes apart, Table 1) is associated with significant errors (±50 %) due to the short duration between the surveys but the calculated flux (0.23 $m^3 s^{-1}$) is in line with the previous and following flux values (0.19 and 0.22 $m^3 s^{-1}$, Figure 6a). Negligible net change was detected between surveys 29c1/2 and 29c3, suggesting that flow front 3 may have stopped. Although this was the last survey pair carried out, the flow was observed to have continued to advance when visited the next day. Unfortunately, the overnight advance (29 – 30 September) overran the control targets deployed, so calculation of a final flux value was not possible.

4.3 Channel fluxes and rheology

For data from 27 September, the average flow-front flux values can be compared with channel fill levels (as a proxy for lava flux) determined from the thermal image sequence (from which excerpts are shown in Figure 5). Figure 6b shows data from two points (labelled in Figure 5, panel i) on the channels feeding both flow-fronts 1 and 2. For flow-front 1, the upstream channel point (1a) indicated height changes of ~5 m and the downstream point (1b) varied by less than 2 m. For the channel feeding flow-front 2, the smaller channel produced larger height changes, with over 7 m occurring as the pulse front passed. On both channels, the distance between the points chosen was ~50 m and, with a lag of approximately 30 minutes between the up- and downstream changes, this gives a descent rate of the pulses of ~1.6 $m\,min^{-1}$.

For the flow-front 2 channel, the favourable viewing geometry allowed the optical flow technique to be applied to a sequence of thermal images collected over a 9-minute period (11:57 – 12:06, 27 September) of relatively steady flow (Figure 7). The underlying channel topography (including levees) was constrained by a survey carried out around 3 pm on 28 September (survey 28b, Table 1), under conditions of near complete channel drainage. For the period of the thermal image sequence, the location of the lava surface was determined by reprojecting the image position of the eastern edge of the flow onto the levee topography. With the western channel margin being much less distinct, the flow surface was then defined by planes which passed through the defined points on the eastern flow edge and had dip directions parallel to the channel, i.e. they were horizontal across the channel (Figure 7a, inset).

The average optical flow was calculated from 17 sequential image pairs taken at intervals of 30 s around 12:00, 27 September. The resulting flow vectors (in image space) were then transformed into object space by reprojection onto the modelled flow surface (Figure 7b). In the figure, the edges of the channel are indicated by the regions of elevated apparent temperature, indicative of the channel margin shear disrupting the relatively cool flow surface and exposing hotter, deeper material. Note that velocity vectors of non-negligible magnitude are also present outside of the channel region, suggesting motion of the levees. This is an artifact of optical flow schemes, which use a smoothness constraint (e.g. minimising the square of the optical flow velocity gradient magnitude [*Horn and Schunck*, 1981]) to regularise the output displacement field in order to determine a unique optimum solution. A consequence of this is the blurring of velocities into areas of low intensity contrast and here, the channel velocities propagate into the (stationary and lower-contrast) levee areas. This has the effect of the apparent widening of cross-channel velocity profiles and inducing some asymmetry in the profiles, dependent on the image contrast in the levee regions (Figure 7c). Within the channel region, the velocity field has been verified by integrating the individual optical flow results for each image pair in the sequence and observing that, with the exception of at the margins, the displacements produced follow the lava surface motion. Thus, although velocity profiles are distorted toward their edges, and hence are not used further here, velocity magnitudes for the central channel are believed to have been accurately recovered. Imaging the channel more closely (or with the use of a narrower angle lens) would have allowed significantly better velocity profiles to have been calculated because the edge effects would represent a smaller proportion of the channel width.

A rigorous error metric for the velocities is difficult to determine due to the number of different steps involved. However, estimates can be made to illustrate the appropriate magnitudes. For the points used in the channel topography, average coordinate precisions (derived from the photogrammetry) are 0.07, 0.45 and 0.07 m in X, Y and Z respectively. The disproportionately large value in the Y direction is due to the optical axes for the images used being close to that direction. Observing slopes inclined by up to 34° along the Y direction could increase the error in the local Z values determined by 0.3 m. Hence, a conservative error of 0.5 m in height could be used to incorporate uncertainties in the initial topography and the position of the lava surface.

In order to estimate error in the movement vectors computed using optical flow for the channel region, the magnitude of vectors generated in areas of the image where the surface is stationary can be considered. In making this analysis, areas of similar contrast variation to those of interest should be used. Within the sequence investigated, the only such areas are the relatively small areas of warm levee observed. For 100 ‘zero-velocity’ vectors in the stationary levee area, the root mean square of the displacement magnitudes was 0.02 pixels. In the channel regions, at the relevant distances and angles, the thermal image pixels reprojected onto the topography have footprints between 0.9 and 1.3 m in the down-channel direction. Hence, a 0.02 pixel error represents ~0.02 m on the surface and, with images taken at 30 s intervals, this implies a 0.04 $\mathrm{m\,min^{-1}}$ error magnitude in velocities from the optical flow process. This increases to 0.05 $\mathrm{m\,min^{-1}}$ if an estimated uncertainty of ±5° in the local slope is included.

Given a number of assumptions, the flow velocity results can be used to estimate lava flux and rheological properties. For the simplest approach the lava is assumed to be Newtonian fluid, unimpeded by any surface crust, and flowing in a wide channel of rectangular cross section. For steady flow and a flow depth perpendicular to the flow surface, *h*, the Newtonian viscosity, η_N, can be calculated from the maximum surface velocity, v_{max}, by

$$\eta_N = \frac{\rho g \sin\alpha}{2 v_{max}} h^2 \qquad 1),$$

where ρ, α and g are the fluid density, channel slope and gravitational acceleration respectively [*Dragoni et al.*, 1995]. Flux, Q_N, is given by

$$Q_N = \tfrac{2}{3} v_{max} h w \qquad 2),$$

where *w*, is the channel width. In Table 2, flux values have been calculated for three channel cross sections (A, B and C, in Figure 7b), assuming constant values of $\rho = 2000$ kg m^{-3} and $g = 9.8$ m s^{-2}. The sensitivity of the results to errors in velocity and flow depth has been illustrated by providing minima and maxima bounds determined by 0.05 m min^{-1} and ± 0.5 m variations in velocity and flow depth respectively. The results from sections B and C are in good agreement (0.08 and 0.07 m^3 s^{-1}), but differ considerably from those obtained from section A (0.21 m^3 s^{-1}) and an examination of the data indicates an apparent inconsistency. Comparison of the data from A and B indicates that, for a similar gradient, lava in the deeper channel section (A) was flowing slower than in the shallower one (B). Only in the case of significant changes in rheology, channel geometry or lava density could this be possible for steady flow under equilibrium conditions. A more likely alternative is that at A, the flow was not at equilibrium and was accelerating due the recent increase in the gradient, a case for which equation 1 is not valid. Hence, results from section A should be treated with caution.

However, lavas have been previously shown to be non-Newtonian in their behaviour, and are often represented as Bingham fluids [*Robson*, 1967; *Hulme*, 1974; *Pinkerton and Sparks*, 1978]. Bingham models have been derived and discussed in detail elsewhere [*Johnson*, 1970;

Dragoni et al., 1986; *Dragoni et al.*, 1992], so we reproduce rather than re-derive the relevant equations here.

For a wide rectangular channel the maximum flow velocity, at which the plug-flow region travels, is

$$v_{\max} = \frac{1}{2\eta_{\mathrm{B}}}\left(h^2 \rho g \sin\alpha + \frac{K^2}{\rho g \sin\alpha} - 2hK\right) \qquad 3),$$

where η_{B} is the Bingham viscosity and K is the shear strength. The thickness of the plug region, T_c, is given by

$$T_c = \frac{K}{\rho g \sin\alpha} \qquad 4).$$

Equation 3 is usually employed to find the Bingham viscosity, using measurements of the maximum flow velocity and independent measurements of shear strength [*Lipman and Banks*, 1987]. Here, we can use two sets of velocity, slope and height measurements to simultaneously ascertain η_{B} and K. With K to the second power in equation 3, each pair of measurement sets provides two potential solutions of K and η_{B} but, in order for a solution to be valid, it must also satisfy the constraint that the plug depth is smaller than the flow thickness ($T_c < h$). So, from equation 4, solutions not satisfying

$$K < h\rho g \sin\alpha \qquad 5),$$

can be discarded. For valid values of K and η_{B}, the Bingham fluid flux is given by

$$Q_{\mathrm{B}} = \frac{w}{6\eta_B}\left(2h^3 \rho g \sin\alpha + \frac{K^3}{\rho^2 g^2 \sin^2\alpha} - 3Kh^2\right) \qquad 6),$$

Three measurement sets have been obtained from the cross-sections A, B and C. However, due to the belief that at A, the flow is not in equilibrium, η_{B} and K are calculated from measurements at sections B and C only (Table 2). Note that volume conservation is not invoked in solving equation 3, so independent flux measurements for both sections can be made using the rheological parameters determined and these are similar to the values determined using the Newtonian model (0.11 and 0.10 $m^3 s^{-1}$).

For the channel feeding flow front 1, the highly oblique imaging geometry of the upper channel areas combined with extended range (Figure 5) can be expected to produce a relatively inaccurate reprojection of the optical flow vectors onto the 3D surface model. Hence, velocities have not been calculated by this method; however, the undulose topography of the ogives in the lower areas of the channel has allowed an alternative topographic measurement of velocity. The multiple local horizons produced (when observed at a shallow angle from the flow-front viewing position) make the ogive crests readily distinguishable in the topographic data (Figure 8). Individual crests can then be tracked between surveys using the thermal image sequences.

Surveys 27a and 27b reconstructed the most ogives during the survey period, and the average descent of their crests gives a flow velocity of 0.19 m min^{-1}. With an average channel width (from the photogrammetric data) of 19 m and an estimated flow depth of 3 m (the channel was never observed in a fully drained state), equation 2 gives a flux of 0.12 $m^3 s^{-1}$. If variations and uncertainties in the lava depth are estimated to be covered by a range between 2 and 4 m, the corresponding calculated fluxes would be 0.08 – 0.16 $m^3 s^{-1}$, similar to the values calculated for the flow-front 2 channel (Table 2).

5 Discussion

Close-range photogrammetry and computer vision are established fields but the authors are not aware of previous application of the techniques for the measurement of lava flux. Consequently, although most of the data collection problems encountered are well known (e.g. occlusion by local topography or condensing gases) several specific analysis issues encountered are worth highlighting.

For the 'a'ā flow-fronts observed on Etna, with advance rates of a few metres per hour, small scale local changes (e.g. spalling, a block falling or moving suddenly) were sufficiently frequent to influence DEM generation from images. Despite multiple images being usually taken in rapid succession, subtle surface changes often resulted in patches of unmatchable image texture between non-sequentially acquired image pairs. Thus, whilst all relevant images could be utilised within a photogrammetric bundle adjustment solution, in order to provide a common set of camera orientations, image matching for topographic data extraction was often carried out with sequential image pairs.

In some cases, problems were also introduced because of the presence of overhanging blocks. Although such blocks were accurately depicted within point cloud data, overhanging surfaces cannot be represented by the standard interpolation of height (Z) values used in mainstream digital terrain modelling software. A more sophisticated surface reconstruction approach could have been employed (for example Marching Cubes [*Lorensen and Cline*, 1987]), but in view of the simplicity of height interpolation, its ease for volumetric analysis and the relative infrequency of overhanging surfaces, Z-interpolation was used. Consequently, ‘overhung’ data points were manually removed from point clouds before interpolation.

5.1 Lava fluxes and rheology

The lava flux feeding individual flow-front regions has been measured by three independent techniques; topographic change at the flow-fronts, thermal-intensity-derived channel velocities (using optical flow) and topography-derived channel velocities (ogive velocities). Topographic changes of the flow-fronts provide averaged fluxes for the fronts over timescales of hours, with values recorded between 0.35 and <0.05 $m^3 s^{-1}$. For the two active flow-fronts on 27 September, the total flux is <0.5 $m^3 s^{-1}$ which is considerably lower than the average effusion rate for the 2004-2005 eruption (3 $m^3 s^{-1}$, [*Burton et al.*, 2005]). Furthermore, our own observations of near-vent fluxes (on 24 September) suggest that effusion rates for this channel during the period of fieldwork may have been as high as 4 – 5 $m^3 s^{-1}$, giving a large difference between the volumetric fluxes observed at the vent and at the flow-fronts.

For the 'a'ā flows from Mauna Loa in 1984, similar differences were noted with volumetric fluxes of 3.5 – 5 $\times 10^6$ $m^3 hr^{-1}$ measured at the vent, having decreased by more than an order of magnitude when measured 15 km down-channel [*Lipman and Banks*, 1987; *Moore*, 1987]. This decrease was attributed to volatile loss and was accompanied by a several-fold, down-flow increase in lava density (values ranged from ~300 to 2600 $kg\,m^{-3}$ in samples collected between the vent and 16 km down-flow [*Lipman and Banks*, 1987]). The same degassing process will also be a factor at Etna but to a lesser degree, and it is possible that other unmeasured flow-fronts were simultaneously active (such as the one shown in Figure 2d, 29 September). It is also likely that mass loss occurred gradually along the channel by levee-building and overtopping. Hence, we attribute these flux differences dominantly to steady down-channel mass-loss from the channel and to degassing.

In this work, the optical flow method was applied to only a small number of channel images, and the results used to determine rheological parameters and channel flux. However, with the images used taken at a viewing distance of ~200 m and the channel covering only a relatively small number of pixels, there are undesirable geometric uncertainties and the optical flow process deteriorates at the channel margins. Hence, although the value of lava shear strength obtained is in line with previous work on Etna [*Pinkerton and Sparks*, 1978], the Bingham viscosity value determined is associated with significant error. With the narrow range of strain rates occurring, these measurement uncertainties must be reduced in order to increase the accuracy of the rheological calculations. However, this can be achieved by imaging closer to the appropriate flow region, which would also allow full velocity profiles to be accurately measured and hence employed within the rheological and flux modelling. Furthermore, by simultaneously obtaining stereo visible imagery from which a continuously updated lava surface model could be determined, these parameters could be monitored through time in a manner similar to the channel level (Figure 6b) and this is a goal of future work.

5.2 Flux variations

The origin of the flux variations observed in the distal flow regions cannot be precisely determined because it was impossible to simultaneously monitor the entire length of the active channel during the 2004-2005 eruption. However, three types of processes can be considered:

1) Periodic channel processes, such as up-flow levee breaching, or damming of the channel by levee collapse.
2) Sub-surface processes, which result in variation of effusion rate at the vent.
3) Persistent channel processes, such as inherent flow instabilities.

As a periodic channel process, levee breaching is a possible cause of rapid decreases in measured flux, but not for relatively sudden increases in flux, such as pulses. Lava pulses of can be generated by temporary damming of channels (e.g. by parts of collapsing levee walls, [*Guest et al.*, 1987; *Bailey et al.*, 2006]), although this was not observed during time spent in the proximal regions. Thus, in this particular case, it is not thought that periodic channel processes represent the driving mechanism for the distal flux variations measured.

Observations of the lava surface height made near the vent (~200 m down flow of the effusive bocca, 24 September) revealed changes of up to ~0.5 m over time scales of ~30 minutes. These changes were very gradual and were thought to directly reflect variation of the effusion rate in a manner similar to those observed at Etna in 2001 by *Bailey et al*. [2006]. For a simple estimate of the lava volumes involved (neglecting evolving flow profiles and unknown subsurface channel geometry), using a maximum velocity of ~1 m s^{-1} and channel width of ~2 m, then an increase in flow depth of 0.5 m every alternate 15 minutes will represent an additional, ‘excess’ flux of ~1200 m^3 hr^{-1}.

In the distal region, the angle and distance to the main channel (up-slope of the bifurcation) prevented photogrammetric measurement of pulses, so approximations of the dimensions involved have been used in the absence of survey data. Assuming a channel width of ~10 m, a pulse length and height of ~15 × 5 m respectively, and a roughly triangular down-flow profile (see Figure 2c), gives a volume of ~380 m^3. Occurring on the 2 – 4 hour timescale observed of the pulse events in the distal channel region, this represents an average 'pulse' flux of ~130 m^3 hr^{-1}. This is approximately an order of magnitude smaller than the 'excess' flux calculated for the near-vent region, a ratio which is in agreement with that calculated between the average fluxes at the vent and distal regions, as discussed in the previous section. Thus, the distal pulses observed could reflect near-vent fluctuations (possibly resulting from changes in effusion rate), but a mechanism for effectively coalescing these fluctuations as they travel down-channel would have to be invoked.

Persistent channel processes such as inherent flow instabilities represent such a possible process. A scenario can be envisaged in which periods of increased flux generate portions of deeper channel flow which advance more rapidly and cool slower than material erupted during periods of shallower flow. Hence, larger pulses could catch up and 'collect' smaller pulses as they descend. Kinematic wave models of flows [*Baloga and Pieri*, 1986; *Baloga*, 1987] have shown how the evidence of effusive behaviour at one time period can be overrun and buried by subsequent effusive behaviour. This modelling approach could be used to investigate fluxes, flux changes and the effect of non-linear rheologies on the generation of pulses in distal regions, but further investigation is left to future work.

It is interesting to consider if the unsteady flow can be correlated to the production of the observed ogives, which appeared to start where the gradient decreased and the channel widened, supporting the importance of compressive forces in their formation. For a typical ogive in the flow-front 1 channel, with a channel width of ~19 m, an along-channel distance of ~5 m and excess height of 2 m, excess volume is ~200 m^3. With any distal pulse split at the channel bifurcation, this is inline with one channel's portion of a 380 m^3 pulse. Hence, it could be suggested that the ogives may have formed as the remnants of pulses, rather than by compressive terminal processes alone. However, with the ogives moving at ~0.2 m s^{-1}, and separated by ~15 m (Figure 8) they were being formed at a rate of one every hour and a half, approximately twice the rate of the distal pulses. Therefore, although it is difficult to see how flux changes could not influence ogive formation in some manner, and despite individual volumetric similarity, a one-to-one ratio was not evident in the flows observed.

6 Summary

Close-range photogrammetry and computer vision techniques have been demonstrated as useful tools for investigating active 'a'ā lava flows, with the use of image data allowing sufficiently large spatial areas to be surveyed quickly and accurately. The flow-front regions observed on Etna in September 2004 displayed significant variations in flux, resulting from flux variations in the distal channel regions which caused episodic draining and overflowing. Discrete pulses of lava arriving in the distal flow regions were observed on timescales of several hours, and are believed to represent the down-channel coalescence of flow regions erupted at slightly enhanced fluxes. Average volumetric flux at the flow-front region was an order of magnitude smaller than that near the vent and this is attributed to mass loss over levees down the channel system, compounded by volatile loss from the lava.

Acknowledgements

This work was supported by the Royal Society. M. Ball is gratefully acknowledged for his assistance during data collection on Etna. We thank M. Zuliani for sharing the code used for optical flow calculations and H. Tuffen for comments on an early draft of the paper. The manuscript was significantly improved by reviews from J. Kauahikaua and E. Fujita.

References

Bailey, J. E., A. J. L. Harris, J. Dehn, S. Calvari, and S. K. Rowland (2006), The changing morphology of an open lava channel on Mt. Etna, *Bull. Volcanol.*, *68*, 497-515, DOI 410.1007/s00445-00005-00025-00446.

Baloga, S. (1987), Lava flows as kinematic waves, *J. Geophys. Res.*, *92*, 9271-9279.

Baloga, S., and D. Pieri (1986), Time-dependent profiles of lava flows, *J. Geophys. Res.*, *91*, 9543-9552.

Burton, M. R., M. Neri, D. Andronico, S. Branca, T. Caltabiano, S. Calvari, R. A. Corsaro, P. Del Carlo, G. Lanzafame, L. Lodato, L. Miraglia, G. Salerno, and L. Spampinato (2005), Etna 2004-2005: An archetype for geodynamically-controlled effusive eruptions, *Geophys. Res. Lett.*, *32*, L09303.

Calvari, S., M. Neri, and H. Pinkerton (2002), Effusion rate estimations during the 1999 summit eruption on Mount Etna, and growth of two distinct lava flow fields, *J. Volcanol. Geotherm. Res.*, *119*, 107-123.

Cecchi, E., B. van Wyk de Vries, J. M. Lavest, A. Harris, and M. Davies (2003), N-view reconstruction: a new method for morphological modelling and deformation measurement in volcanology, *J. Volcanol. Geotherm. Res.*, *123*, 181-201.

Chandler, J., P. Ashmore, C. Paola, M. Gooch, and F. Varkaris (2002), Monitoring river-channel change using terrestrial oblique digital imagery and automated digital photogrammetry, *Annals of the Association of American Geographers*, *92*, 631-644.

Crisci, G. M., S. Gregorio, R. Rongo, M. Scarpelli, W. Spataro, and S. Calvari (2003), Revisiting the 1669 Etnean eruptive crisis using a cellular automata model and implications for volcanic hazard in the Catania area, *J. Volcanol. Geotherm. Res.*, *123*, 211-230.

Davies, E. R. (2005), *Machine Vision*, 934 pp., Morgan Kaufmann Publishers, San Francisco, CA.

Dragoni, M., M. Bonafede, and E. Boschi (1986), Downslope flow models of a bingham liquid - implications for lava flows, *J. Volcanol. Geotherm. Res.*, *30*, 305-325.

Dragoni, M., A. Piombo, and A. Tallarico (1995), A model for the formation of lava tubes by roofing over a channel, *J. Geophys. Res.*, *100*, 8435-8447.

Dragoni, M., S. Pondrelli, and A. Tallarico (1992), Longitudinal deformation of a lava flow - The influence of Bingham rheology, *J. Volcanol. Geotherm. Res.*, *52*, 247-254.

Frazzetta, G., and R. Romano (1984), The 1983 Etna eruption: event chronology and morphological evolution of the lava flow, *Bull. Volcanol.*, *47*, 1079-1096.

Guest, J. E., C. R. J. Kilburn, H. Pinkerton, and A. M. Duncan (1987), The evolution of lava flow-fields: observations of the 1981 and 1983 eruptions of Mount Etna, Sicily, *Bull. Volcanol.*, *49*, 527-540.

Harris, A., J. Dehn, M. Patrick, S. Calvari, M. Ripepe, and L. Lodato (2005), Lava effusion rates from hand-held thermal infrared imagery: an example from the June 2003 effusive activity at Stromboli, *Bull. Volcanol.*, *68*, 107-117.

Harris, A. J. L., L. P. Flynn, L. Keszthelyi, P. J. Mouginis-Mark, S. K. Rowland, and J. A. Resing (1998), Calculation of lava effusion rates from Landsat TM data, *Bull. Volcanol.*, *60*, 52-71.

Harris, A. J. L., J. B. Murray, S. E. Aries, M. A. Davies, L. P. Flynn, M. J. Wooster, R. Wright, and D. A. Rothery (2000), Effusion rate trends at Etna and Krafla and their implications for eruptive mechanisms, *J. Volcanol. Geotherm. Res.*, *102*, 237-270.

Hidaka, M., A. Goto, S. Umino, and E. Fujita (2005), VTFS project: Development of the lava flow simulation code LavaSIM with a model for three-dimensional convection, spreading, and solidification, *Geochemistry Geophysics Geosystems*, *6*, Q07008.

Horn, B. K. P., and B. G. Schunck (1981), Determining optical-flow, *Artificial Intelligence*, *17*, 185-203.

Hulme, G. (1974), The interpretation of lava flow morphology, *Geophys. J. Roy. Astron. Soc.*, *39*, 361-383.

Hunter, G., H. Pinkerton, R. Airey, and S. Calvari (2003), The application of a long-range laser scanner for monitoring volcanic activity on Mount Etna, *J. Volcanol. Geotherm. Res.*, *123*, 203-210.

James, M. R., S. Robson, H. Pinkerton, and M. Ball (2006), Oblique photogrammetry with visible and thermal images of active lava flows, *Bull. Volcanol.*, DOI 10.1007/s00445-00006-00062-00449.

Johnson, A. M. (1970), *Physical processes in geology*, 577 pp., Freeman, Cooper & Company, San Francisco, California.

Kilburn, C. R. J., and R. M. C. Lopes (1988), The growth Of aa lava flow-fields on Mount Etna, Sicily, *J. Geophys. Res.*, *93*, 14759-14772.

Lautze, N. C., A. J. L. Harris, J. E. Bailey, M. Ripepe, S. Calvari, J. Dehn, S. K. Rowland, and K. Evans-Jones (2004), Pulsed lava effusion at Mount Etna during 2001, *J. Volcanol. Geotherm. Res.*, *137*, 231-246.

Lipman, P. W., and N. G. Banks (1987), 'A'ā flow dynamics, Mauna Loa 1984, in *Volcanism in Hawaii*, edited by R. W. Decker, et al., pp. 1527-1567.

Lorensen, W. E., and H. E. Cline (1987), Marching cubes: A high resolution 3D surface construction algorithm, *Computer Graphics*, *21*, 163-169.

Lucas, B. D., and T. Kanade (1981), An iterative image registration technique with an application to stereo vision, paper presented at Proceedings of the 7th International Joint Conference on Artificial Intelligence, Vancouver.

Macfarlane, D. G., G. Wadge, D. A. Robertson, M. R. James, and H. Pinkerton (2006), Use of a portable topographic mapping millimetre wave radar at an active lava flow, *Geophys. Res. Lett.*, *33*, L03301.

Mazzarini, F., M. T. Pareschi, M. Favalli, I. Isola, S. Tarquini, and E. Boschi (2005), Morphology of basaltic lava channels during the Mt. Etna September 2004 eruption from airborne laser altimeter data, *Geophys. Res. Lett.*, *32*, Art. no. L04305.

Moore, H. J. (1987), Preliminary estimates of the rheological properties of 1984 Mauna Loa Lava, in *Volcanism in Hawaii*, edited by R. W. Decker, et al., pp. 1569-1587.

Neal, C. A., and R. W. Decker (1983), Surging of lava flows at Kilauea volcano, Hawaii, *Eos, Trans. AGU*, *64*, 904.

Papadaki, H. (2002), Accuracy of dense surface measurements in an integrated photogrammetry and machine vision framework, *Int. Arch. Photogram. Remote Sensing*, *34*, 68-73.

Pinkerton, H., and R. S. J. Sparks (1976), The 1975 sub-terminal lavas, Mount Etna: Case history of formation of a compound lava field, *J. Volcanol. Geotherm. Res.*, *1*, 167-182.

Pinkerton, H., and R. S. J. Sparks (1978), Field measurements of the rheology of lava, *Nature*, *276*, 383-385.

Pinkerton, H., and L. Wilson (1994), Factors controlling the lengths of channel-fed lava flows, *Bull. Volcanol.*, *56*, 108-120.

Robson, G. R. (1967), Thickness of Etnean lavas, *Nature*, *216*, 251-252.

Wadge, G., D. Oramas Dorta, and P. D. Cole (2006), The magma budget of Volcán Arenal, Costa Rica from 1980 to 2004, *J. Volcanol. Geotherm. Res.*, *157*, 60-74.

Walker, G. P. L. (1972), Compound and simple lava flows and flood basalts, *Bull. Volcanol.*, *35*, 579-590.

Walker, G. P. L. (1973), Lengths of lava flows, *Philos. Trans. R. Soc. Lond. Ser. A-Math. Phys. Eng. Sci.*, *274*, 107-118.

Figures

Figure 1. Lava flows at Mount Etna, Sicily in September 2004. The main figure shows the final extent of the 2004-2005 flow-field in black and the inset gives the extent during the fieldwork period. Marks around the southern flow-fronts provide the approximate location of some of the control targets deployed. Reproduced from *James et al.* [2006] with kind permission of Springer Science and Business Media.

Figure 2. Images of the channels and flow-fronts taken looking north from a distance of ~700 m. In (a) an image taken during a period of good visibility shows the two active flow-fronts (flow-fronts 1 and 2, with a total width of ~70 m) on 28 September. The northern wall of the Valle del Bove is seen in the far background, behind Monte Centenari. In (b-d) aligned thermal image composites demonstrate the active flow-fronts (labelled 1 – 3) on each day. The most eastern flow, which is only just visible against the background (and is unlabelled), was observed being emplaced on 23rd September. In (d) a new flow-front to the north can just be observed behind the recent flows, although its channel is obscured from view.

Figure 3. Evolution of the observed flow-fronts as mapped from photogrammetry data. The advancing flow outlines are labelled corresponding to the survey IDs in Table 1. Dashed lines represent inferred rather than observed locations. The positions of control targets are indicated by black squares (wide network), blue circles (intermediate network) and red circles (small network). Several additional targets within the wide network were placed at locations further east, outside the bounds of the figure. A selection of the camera positions used to produce the topographic data is indicated with green triangles. Their irregular distribution reflects the uneven nature of the topography which prevented equal access over the entire area.

Figure 4. Flow surface reconstructions. (a) An overview (27 September) covering the active channel and flow-front areas. Horizontal ticks are every 50 m and the vertical scale gives altitude in metres. This overview covers a much wider area than those used to calculate flow-front fluxes (e.g. (d)) and the darker, irregular region towards the western edge of the reconstruction is the vegetation-covered end of the Serra Giannicola Grande (see Figure 2a). The white line indicates the positions of the cross sections given in (b) through surfaces constructed from surveys carried out on the 27 September (Table 1). The three sections (through static ground) illustrate the repeatability of the results. (c) A typical image of flow-front 3 (taken during Survey 29b2 but partially cropped for the figure). Arrows indicate the positions of the control targets (from the small network) and the distance between the two targets with flagged arrows is 21 m. A perspective view of the flow-front model produced in Survey 29c1/2 (with mesh lines at 0.4 m intervals) is given in (d). Horizontal ticks are every 5 m and the mesh is shaded by height change since Survey 29b2, which had been carried out an hour previously. Note the lobate nature of the height change, illustrating the uneven nature of the flow advance since Survey 29b2 (when the morphology was much like that seen in (c)).

Figure 5. Thermal images showing the descent of a lava pulse on 27 September. The camera was looking approximately due north and local times are given in the top right of each panel. For scale, the left-hand channel is approximately 10 m in width (see Figure 3). The two-channel region shown in each panel can be put in context by comparing with the wider view in Figure 2b. The points labelled in the first panel correspond to areas where the channel fill level was tracked throughout the thermal sequence (Figure 6b). Arrows in panels ii – v indicate the position of the pulse front as it enters the bifurcation (ii) and descends the flow-front 2 channel (iii – v). See text for discussion of the pulse sequence illustrated.

Figure 6. Mean volumetric fluxes at flow-fronts and variation of channel fill levels. (a) Calculated flux values between topographic surveys for the three flow-fronts monitored. Each black horizontal line gives the flux value calculated between surveys carried out at the times indicated by the start and end positions of the line. The surrounding grey bands show the estimated worst-case error bounds (see text for details). The survey IDs (see Table 1) are marked on the top axis at their appropriate times. Note the large error estimate between surveys 29b1 and 29b2 due to the very short duration between these surveys (5 minutes, Table 1). (b) Channel fill levels (taken from arbitrary origins) for two points on both channels. The point positions are labelled in the first panel image of Figure 5 and the data gap around 12:30 results from poor visibility due to cloud. A further data gap in the 2a trace around 15:45 resulted from the point tracked being obscured by the body of the pulse as it passed.

Figure 7. Channel surface velocities from optical flow. (a) The first image of the 18-image sequence from which the average optical flow was calculated. The inset shows the region of interest on the flow-front 2 channel, with the calculated lava surface model overlain. In (b), this lava surface model has been used to orthorectify the thermal data and the overlain flow vectors. For clarity, only a small proportion of the velocity vectors are plotted and the dashed lines represent the channel margins (as determined from the thermal image sequence). The left-hand panel shows topographic cross-sections taken perpendicular to the channel obtained from visible images taken on 28 September during a period of channel drainage (note the ×3 vertical exaggeration). The calculated lava surface is shown in red. In (c), surface channel velocity profiles taken along sections A, B, and C in (b) are plotted. The channel margin positions as indicated in (b) are given by the circles. Note that projecting the data onto a planar surface (i.e. disregarding the levee topography) exaggerates the horizontal scale in the levee regions. This, in conjunction with any vertical error, is the reason why channel widths suggested by the orthorectified thermal image data appear greater than those in the topographic cross sections.

Figure 8. Down-flow sections through the flow-front 1 channel, 27 September. Black line segments represent topography from survey 27a (12:17, Table 1), grey segments are from survey 27b (78 minutes later), and the dashed line shows an estimate of the underlying topography. Line segments are only shown for regions visible from the camera positions (i.e. there are no interpolated regions); ‘missing’ segments are unobserved due to the oblique viewing geometry and the undulose nature of the flow surface. The observed regions represent the leading faces and crests of ogives, hence their changing position (tracked in thermal image sequences and shown by the arrows) can be used to estimate flow velocity.

Table 1. Details of the photogrammetric surveys carried out. Survey times are given in local time and quoted for the middle period of the survey. The survey duration was calculated from the timestamps of the first and last image used in each survey. Flow-front numbers and survey IDs correspond to the labelling on Figures 2 and 3.

Date	Survey ID	Survey time (duration, min.)	No. of images used for DEM	Flow-fronts surveyed	Duration between surveys (min.)
27/09/2004	27a	12:17 (2)	4	1, 2	
					78
	27b	13:35 (6)	4	1, 2	
					84
	27c	14:59 (3)	2	1	
					1186
28/09/2004	28a	10:45 (10)	6	1, 2	
					265
	28b	15:10 (5)	4	1	
					1288
29/09/2004	29a	12:38 (2)	4	3	
					40
	29a2	13:18 (2)	2	3	
					100
	29b1	14:58 (4)	2	3	
					5
	29b2	15:03 (3)	6	3	
					58
	29c1/2	16:01 (2)	2	3	
					15
	29c3	16:16 (2)	2	3	

Table 2. Rheological parameters and flux values calculated from the topographic and velocity cross-sections (Figure 4b).

	Cross-section[a]	**A**	**B**	**C**
	Slope, α, (°)	34	33	22
	Max. velocity magnitude, v_{max}, (m min^{-1})	1.2	1.5	0.9
	Flow depth, h (m)	2.1	0.8	1.1
	Flow width, w (m)	6.5	4.5	6.0
Newtonian model	Newtonian viscosity[b], η_{N}, (M Pa s)	1.0 {0.6 – 1.6}	0.12 {0.02 – 0.30}	0.30 {0.09 – 0.66)
Newtonian model	Flux[b], Q_{N}, (m^3 s^{-1})	0.21 {0.16 – 0.25}	0.08 {0.03 – 0.12}	0.07 {0.04 – 0.09}
Bingham model	Shear strength[b], K, (k Pa)		7.8[c] {6.3 – 13}	
Bingham model	Bingham viscosity[b], η_{B}, (k Pa s)		2.9[c] {0.001[d] – 53}	
Bingham model	Flux[b], Q_{B}, (m^3 s^{-1})		0.11[c] {0.08[d] – 0.17}	0.10[c] {0.08[d] – 0.14}

[a] As labelled in Figure 4b.
[b] Values in curly brackets give the upper and lower bounds, calculated by varying h and v_{max} (see text).
[c] The average of two valid solutions from equation 3.
[d] No valid lower-bound solution exists for an error in h of 0.5 m. This solution was calculated for an error of 0.25 m.

Figure 1 James et al.

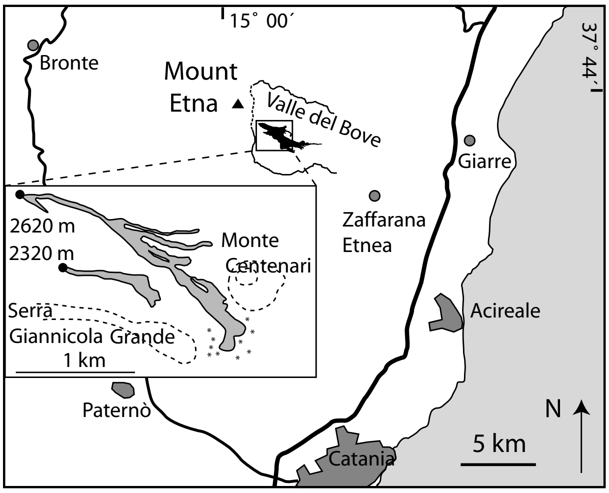

Figure 2. James et al.

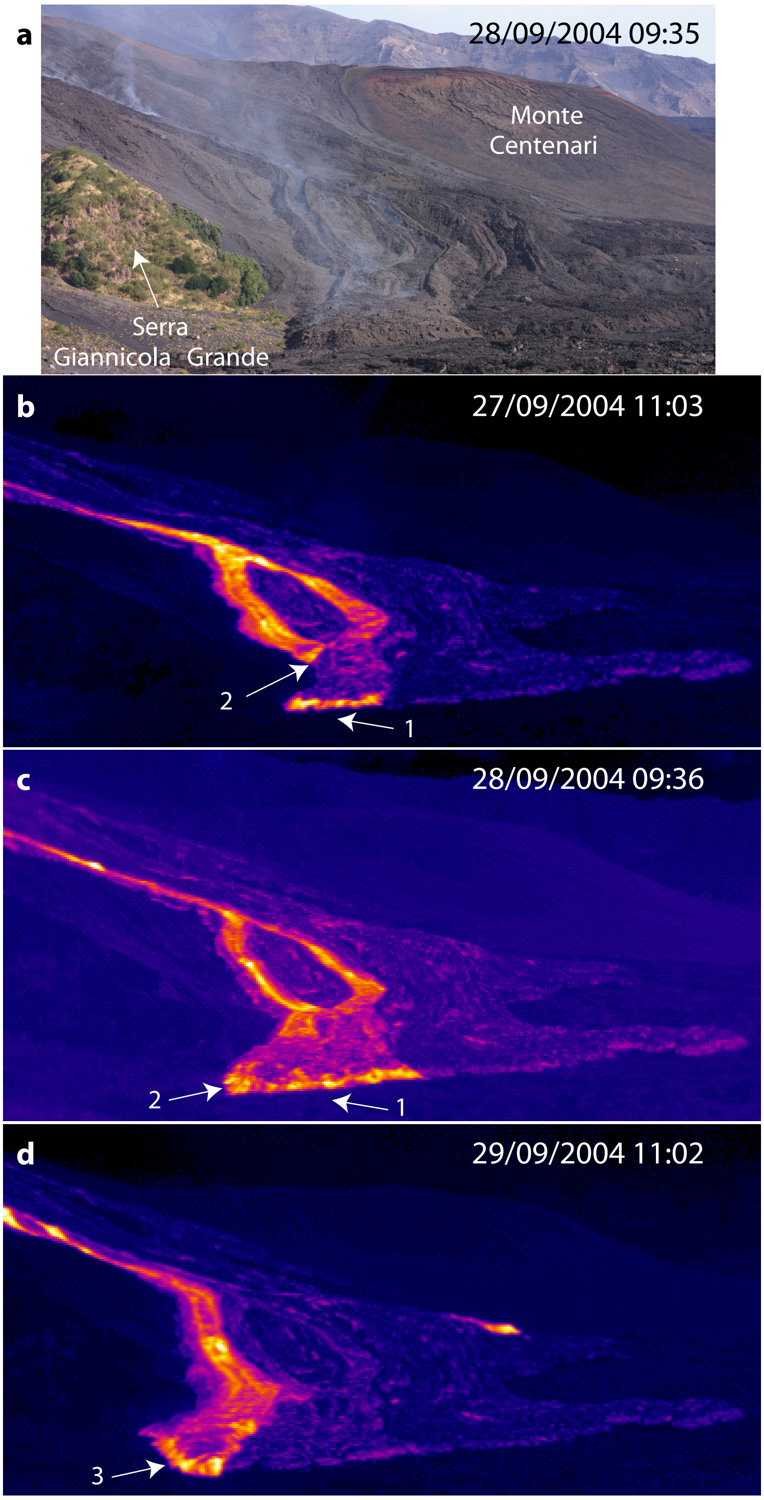

Figure 3. James et al.

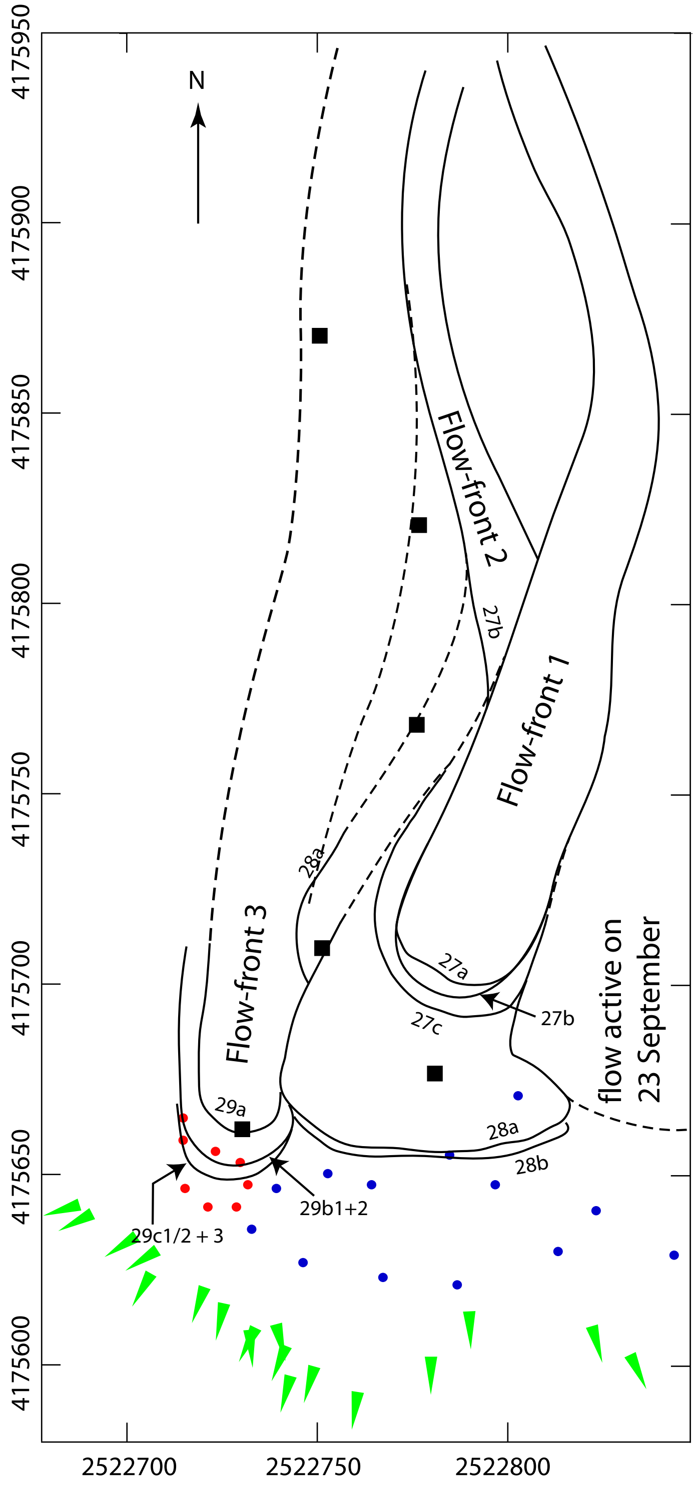

Figure 4 James et al.

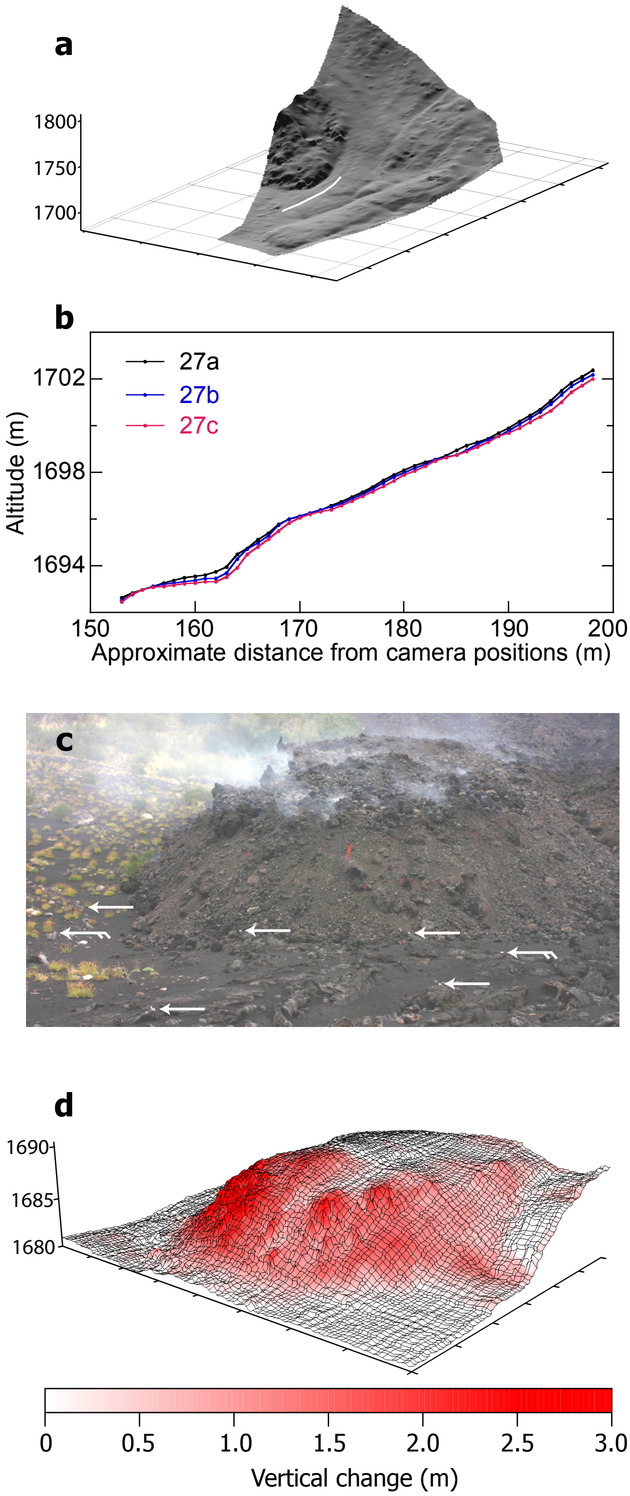

Figure 5. James et al.

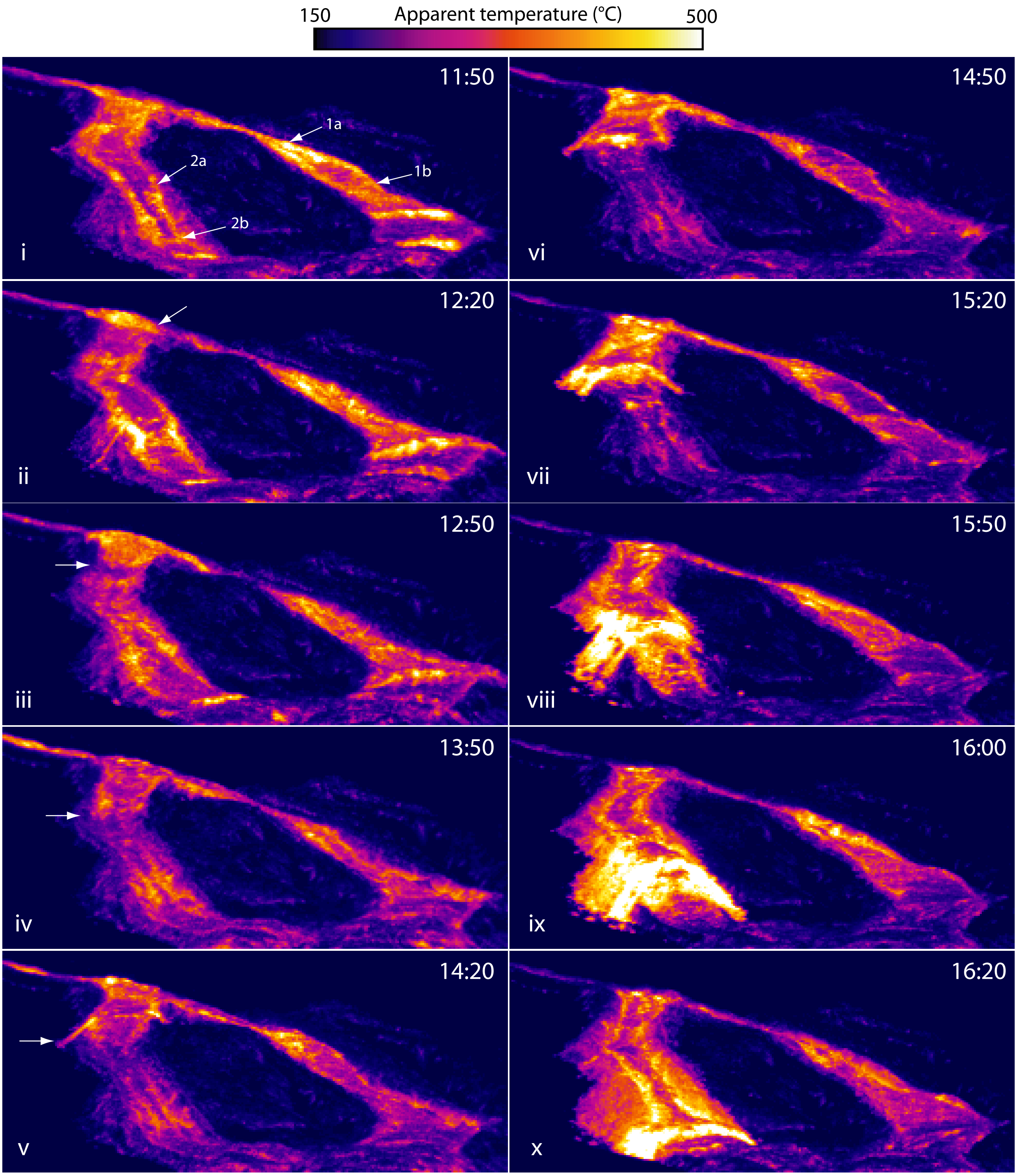

Figure 6. James et al.

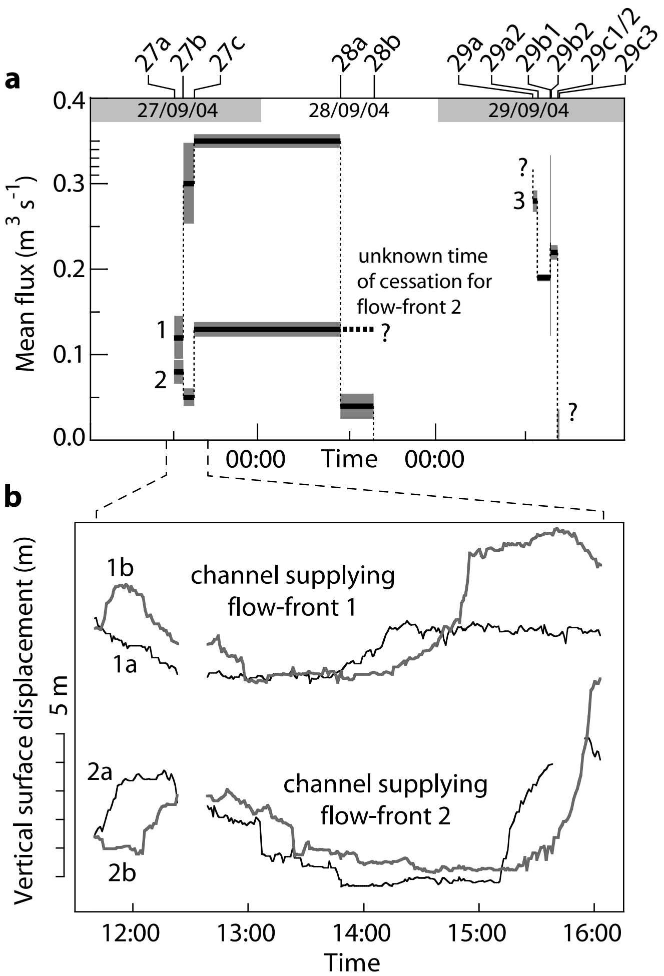

Figure 7. James et al.

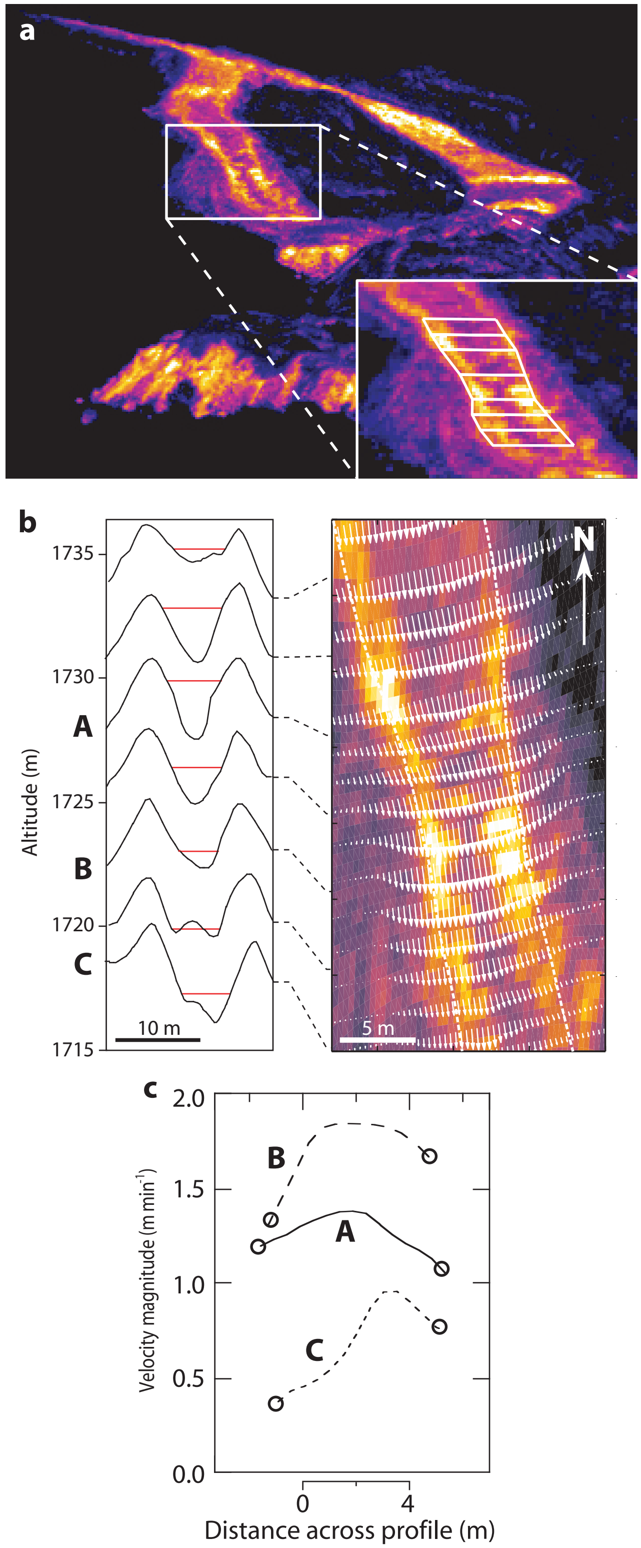

Figure 8. James et al.